Human iPSC-derived Astrocytes Transplanted into the Mouse Brain Display three Morphological Responses to Amyloid-β Plaques

Pranav Preman
   KU Leuven University: Katholieke Universiteit Leuven

Julia TCW
   Mount Sinai School of Medicine: Icahn School of Medicine at Mount Sinai

Sara Calafate
   KU Leuven University: Katholieke Universiteit Leuven

An Snellinx
   KU Leuven University: Katholieke Universiteit Leuven

Maria Alfonso-Triguero
   Achucarro

Nikky Corthout
   KU Leuven University: Katholieke Universiteit Leuven

Sebastian Munck
   KU Leuven University: Katholieke Universiteit Leuven

Dietmar Rudolf Thal
   KU Leuven University: Katholieke Universiteit Leuven

Alison Goate
   Mount Sinai School of Medicine: Icahn School of Medicine at Mount Sinai

Bart Destrooper
   VIB Onderzoekscentrum voor Ontstaansmechanismen van Ziekten: Katholieke Universiteit Leuven Centrum Menselijke Erfelijkheid

Amaia M Arranz (✉ amaia.arranz@achucarro.org)
   Achucarro   https://orcid.org/0000-0002-8314-7870

Research article

Human iPSC-derived astrocytes transplanted into the mouse brain display three morphological responses to amyloid-β plaques

Pranav Preman[1 2 +], Julia TCW[3 4 +], Sara Calafate[1 2], An Snellinx[1 2], Maria Alfonso-Triguero[5], Nikky Corthout[1 2 6], Sebastian Munck[1 2 6], Dietmar Rudolf Thal[7], Alison M Goate[3 4 8], Bart De Strooper[1 2 9 *] and Amaia M Arranz[1 2 5 10 *]

[1] VIB Center for Brain & Disease Research, Leuven, Belgium.

[2] Laboratory for the Research of Neurodegenerative Diseases, Department of Neurosciences, Leuven Brain Institute (LBI), KU Leuven (University of Leuven), Leuven, Belgium.

[3] Department of Neuroscience & Friedman Brain Institute, Icahn School of Medicine at Mount Sinai, New York, NY, United States of America.

[4] Ronald M. Loeb Center for Alzheimer's disease, Icahn School of Medicine at Mount Sinai, New York, NY, United States of America.

[5] Achucarro Basque Center for Neuroscience, Leioa, Spain.

[6] VIB Bio Imaging Core, Campus Gasthuisberg, 3000, Leuven, Belgium.

[7] Laboratory for Neuropathology, Department of Imaging and Pathology, Leuven Brain Institute (LBI), KU Leuven (University of Leuven); and Department of Pathology, University Hospital Leuven, Leuven, Belgium.

[8] Department of Genetics and Genomic Sciences, Icahn Institute of Genomics and Multiscale Biology, Icahn School of Medicine at Mount Sinai, New York, NY, United States of America.

[9] UK Dementia Research Institute, University College London, London, UK.

[10] Ikerbasque Basque Foundation for Science, Bilbao, Spain.

pranav.preman@kuleuven.be

julia.tcw@mssm.edu

sara.calafate@kuleuven.be

an.snellinx@kuleuven.be

28   maria.alfonso@achucarro.org

29   nikky.corthout@kuleuven.be

30   sebastian.munck@kuleuven.be

31   dietmar.thal@kuleuven.be

32   alison.goate@mssm.edu

33   bart.destrooper@vib.be

34   amaia.arranz@achucarro.org

35

36   +These authors contributed equally.

37   * Correspondence: bart.destrooper@vib.be, amaia.arranz@achucarro.org

38

39

40

41

42

43

44

45

46

47

48

49

50

51

ABSTRACT

Background: Increasing evidence for a direct contribution of astrocytes to neuroinflammatory and neurodegenerative processes causing Alzheimer's disease comes from molecular studies in rodent models. However, these models may not fully recapitulate human disease as human and rodent astrocytes differ considerably in morphology, functionality, and gene expression.

Methods: To address these challenges, we established an approach to study human astroglia within the context of the mouse brain by transplanting human induced pluripotent stem cell (hiPSC)-derived glia progenitors into neonatal brains of immunodeficient mice.

Results: Xenografted (hiPSC)-derived glia progenitors differentiate into astrocytes that integrate functionally within the mouse host brain and mature in a cell-autonomous way retaining human-specific morphologies, unique features and physiological properties. In Alzheimer's chimeric brains, transplanted hiPSC-derived astrocytes respond to the presence of amyloid plaques with various morphological changes that seem independent of the *APOE* allelic background.

Conclusion: In sum, this chimeric model has great potential to analyze the role of patient-derived and genetically modified astroglia in Alzheimer's disease.

Keywords: human induced pluripotent stem cells (hiPSCs), astrocytes, chimeric mouse models, Alzheimer's disease, amyloid plaques, *APOE*

BACKGROUND

Astrocytes are essential to maintain the homeostasis of the brain, provide trophic support, stimulate synaptogenesis and neurotransmission, and regulate blood-brain-barrier permeability (1,2). Impaired astroglial function contributes to neurological and neurodegenerative disorders including Alzheimer's disease (AD) (3–8). Genome-wide association studies (9,10) show that genetic risk of AD is also associated with genes mainly expressed in astroglia such as Clusterin (*CLU*), Fermitin family member 2 (*FERMT2*) and Apolipoprotein E (*APOE*) (11), highlighting the potential importance of these cells in the disease. Different types of astroglial pathology have been described in the AD brain (12–14). Among those, hypertrophic (15), quiescent and degenerating morphologies (16,17) were found.

Transgenic models have provided invaluable tools to study the role of astroglia in AD (18–21). However, these models of AD might insufficiently mimic the human disease, as there are major differences between rodent and human astrocytes. Morphologically, human astrocytes are larger and more complex, having around 10 times more processes than their rodent counterparts (22). Molecularly, human astrocytes and mouse astrocytes display different, although overlapping, gene expression profiles (11). Functionally, human astrocytes propagate calcium waves four-fold faster than rodent ones (11,22,23), and human and mouse astrocytes show very different responses when exposed to inflammatory stimuli (24,25).

The ability to generate induced pluripotent stem cells (iPSCs) from patients and differentiate them into astrocytes and other CNS cell types has generated exciting opportunities to examine AD associated phenotypes *in vitro* (39) and unravel the contribution of astroglial risk genes to AD (26–29). Yet, human iPSC (hiPSC)-derived astrocytes grown in culture lack essential components present in the brain which can induce altered phenotypes and gene expression signatures significantly different from that of primary resting astroglia in the brain (11,30).

4

104 Therefore, it has proved challenging to advance understanding of human astroglial function in
105 AD.

106

107 To address these challenges, we aimed at developing a chimeric model that allows studying
108 hiPSC-derived astrocytes in an *in vivo* AD context. We and others have generated chimeric
109 models to study AD by transplanting human PSC-derived neurons or microglia into the brains
110 of immunodeficient AD mice and wild-type littermates (31–33). These models revealed that
111 human neurons and microglia transplanted into the mouse brain respond to pathology
112 differently than their murine counterparts, showing specific vulnerability and transcriptional
113 signatures when exposed to amyloid-β (Aβ) (31,32). Moreover, human glia chimeric mice have
114 been generated by Goldman and collaborators to investigate the function of engrafted human
115 glia, mainly NG2 cells and lower proportions of oligodendrocytes and astrocytes, in disease
116 relevant conditions such as Huntington disease, Schizophrenia or hypomyelination (34–36).
117 Yet, to date no studies have analyzed the phenotype and functional responses of xenografted
118 human astrocytes exposed to Aβ and AD-associated pathology *in vivo.*

119

120 We established here a chimeric model to investigate survival, integration, properties and
121 responses to Aβ species of human astrocytes expressing *APOE* ε3 (E3) vs *APOE* ε4 (E4)
122 variants. We document here engraftment of astrocytes that integrate in a functional way in the
123 mouse host brain and display human-specific morphologies and properties. When transplanted
124 human astrocytes are exposed to Aβ plaques, they display hypertrophic and atrophic
125 responses similar to the ones seen in AD patients' brains (12,16,17). Our results validate the
126 use of chimeric mice as a potential powerful tool for studying astrocyte contribution to AD. We
127 also discuss one of the major hurdles to fully capture the strength of this approach, which is,
128 in our hands, the variable and often low degree of chimerism obtained with human astrocytes
129 from different hiPSC lines after several months of transplantation.

130

METHODS

Generation of isogenic CRISPR/Cas9 gene-edited hiPSCs

Eight hiPSC lines were generated from three *APOE* ε4 carriers diagnosed with AD (Table 1) as described previously by the 'CORRECT' scarless gene-editing method (37). The correct *APOE* sgRNA sequence orientation was confirmed by Sanger sequencing and CRISPR/Cas9-*APOE* sgRNA plasmid cleavage efficiency was determined using the Surveyor mutation detection kit in 293T cells. The single-strand oligo-deoxynucleotide (ssODN) was designed to convert *APOE* ε4 to *APOE* ε3 with a protospacer adjacent motif (PAM) silent mutation to prevent recurrent Cas9 editing. hiPSCs (70-80% confluent) dissociated by Accutase supplemented with 10 µM Thiazovivin (Tzv) (Millipore), were harvested (200 x g, 3 min), and electroporated (Neon®, ThermoFisher) according to the manufacturer's instructions. In brief, cells resuspended in 10µl Neon Resuspension Buffer R, 1µg CRISPR/Cas9-*APOE* sgRNA plasmid and 1µl of 10µM of ssODN were electroporated plated on Matrigel-coated plates in mTeSR media with 10 µM Tzv for 72h. GFP-expressing hiPSC were isolated by FACS (BD FACSAria). Sorted single cells were suspended in mTeSR with Tzv and plated into 96 well plates containing MEFs (4,000 cells/well). Clones were expanded and transferred to a replicate plate for gDNA isolation and Sanger sequencing to identify genome edited clones.

Table 1. Information on the hiPSC lines.

hiPSC line	hiPSC name	Ethnicity	Gender	Age of onset	Age at skin biopsy	Disease status (CDR at biopsy)	APOE genotype	Genetic modification
1	TCW1E33-1F1	Caucasian	F	64	72	AD (2)	E4/E4	E3/E3
2	TCW1E44-2C2	Caucasian	F	64	72	AD (2)	E4/E4	E4/E4
3	TCW2E33-3D11	Caucasian	M	77	80	AD (0.5)	E4/E4	E3/E3
4	TCW2E44-4B12	Caucasian	M	77	80	AD (0.5)	E4/E4	E4/E4
5	TCW2E33-2E3	Caucasian	M	77	80	AD (0.5)	E4/E4	E3/E3

6

6	TCW2E44-4B1	Caucasian	M	77	80	AD (0.5)	E4/E4	E4/E4
7	TCW3E33-H-2	Caucasian	M	80	83	AD (0.5)	E4/E4	E3/E3
8	TCW3E44-F-2	Caucasian	M	80	83	AD (0.5)	E4/E4	E4/E4

150

151 The table shows hiPSC name, patient ethnicity, gender, age of onset, age at skin biopsy,

152 disease status (CDR at biopsy), original *APOE* genotype and genetic modification. F female,

153 M male, AD Alzheimer's disease, APOE apolipoprotein, CDR clinical dementia rating, hiPSC

154 human induced pluripotent stem cells. These cells were previously generated and

155 characterized by (29).

156

157 **Karyotyping**

158 Karyotyping was performed by Wicell Cytogenetics (Madison, WI). Karyotypes are shown in

159 Additional file 2, Figure S1.

160

161 **Generation of reporter hiPSC-astrocytes**

162 The consent for reprogramming human somatic cells to hiPSC was carried out on ESCRO

163 protocol 19-04 at Mount Sinai (J.TCW.). hiPSCs maintained on Matrigel (Corning) in mTeSR1

164 (StemCell Technologies) supplemented with 10 ng/ml FGF2 StemBeads (StemCultures) were

165 differentiated to neural progenitor cells (NPCs) by dual SMAD inhibition (0.1µM LDN193189

166 and 10µM SB431542) in embryoid bodies (EB) media (DMEM/F12 (Invitrogen, 10565), 1x N2

167 (Invitrogen, 17502-048), and 1x B27-RA (Invitrogen, 12587-010)). Rosettes were selected at

168 14 DIV by Rosette Selection Reagent (StemCell Technologies) and patterned to forebrain

169 NPCs with EB media containing 20ng/ml FGF2 (Invitrogen). NPCs (CD271$^-$/CD133$^+$) were

170 enriched by magnetic activated cell sorting (Miltenyi Biotec) (38) and validated

171 immunocytochemically using SOX2, PAX6, FoxP2 and Nestin (Additional file 1, Table S1).

172 Dissociated single cell forebrain NPCs were plated 1,000,000 cells/well on 12 well plates and

173 transfected with lentiGuide-tdTomato (Addgene #99376) plasmid and selected by

174 hygromycine. Pure fluorescent expressing NPCs were plated at low density (15,000 cells/cm^2)

175 on matrigel coated plates and differentiated to astrocytes in astrocyte medium (ScienCell,

176 1801) as described (39). Cells were cultured and harvested as astroglia progenitors at DIV 40-

177 44, validated immunocytochemically and/or by FACS for the astrocyte-specific markers and

178 used for subsequent experiments.

179

180 **AD and WT Immunodeficient Mice**

181 Mice were generated as described previously (31). Briefly, APP PS1 tg/wt mice (expressing

182 KM670/671NL mutated APP and L166P mutated PS1 under the control of the Thy1.2

183 promoter1.1) (40) were crossed with the immunodeficient NOD-SCID mice (NOD.CB17-

184 Prkdc^{scid}) that carry a single point mutation in the Prkdc gene (41). APP PS1 tg/wt Prkdc$^{scid/+}$

185 mice from the F1 generation were crossed with NOD-SCID mice to generate APP PS1 tg/wt

186 Prkdc$^{scid/scid}$ immunodeficient mice. APP PS1 tg/wt Prkdc$^{scid/scid}$ mice were subsequently

187 crossed with NOD-SCID mice to generate either APP PS1 tg/wt Prkdc$^{scid/scid}$ (AD mice) or APP

188 PS1 wt/wt Prkdc$^{scid/scid}$ (WT mice) used for transplantations. Mice were housed in IVC cages in

189 a SPF facility; light/dark cycle and temperature were always monitored. After weaning, no more

190 than five animals of the same gender were kept per cage. Genotyping was done as previously

191 described (31). Transplantation experiments were performed in both male and female

192 littermates at P0-P4. Mouse work was performed in accordance with institutional and national

193 guidelines and regulations, and following approval of the Ethical Committee of the KUL. All

194 experiments conform to the relevant regulatory standards.

195

196 **Intracerebral Grafting**

197 Grafting experiments of hiPSC-derived glial progenitors using neonatal APP PS1 tg/wt NOD-

198 SCID (AD mice) and APP PS1 wt/wt NOD-SCID (WT mice) at postnatal days P0-P4 were

199 performed as described previously (31) with some modifications. Briefly, hiPSC-derived glia

200 progenitor cells at DIV 44 were enzymatically dissociated, supplemented with HB-EGF (100-

47, Peprotech) and RevitaCell (A2644501, ThermoFisher) and injected into the frontal cortex of AD or WT mice. The pups were anesthetized by hypothermia and about 200,000 cells were injected with Hamilton syringes into the forebrain at two locations: 1 mm posterior Bregma, 1.5 mm bilaterally from the midline and 1.2 mm from the pial surface. Transplanted pups were returned to their home cages until weaning age.

Electrophysiological Characterization of Human Glia in Chimeric Mice

Four to five month-old WT mice were anesthetized with isoflurane and decapitated. Acute 300 µm-thick coronal slices were cut on a Leica VT1200 vibratome in a sucrose-based cutting solution consisting of (mM): 87 NaCl, 2.5 KCl, 1.25 NaH2PO4, 10 glucose, 25 NaHCO3, 0.5 CaCl2, 7 MgCl2, 75 sucrose, 1 kynurenic acid, 5 ascorbic acid, 3 pyruvic acid (pH 7.4 with 5% CO2/ 95% O2). Slices were allowed to recover at 34ºC for 45 minutes and maintained at room temperature (RT) in the same solution for at least 30 minutes before using. During recordings, slices were submerged in a chamber (Warner Instruments) perfused with 3-4mL/min artificial cerebrospinal fluid (ACSF) consisting of (mM): 119 NaCl, 2.5 KCl, 1 NaH2PO4, 26 NaHCO3, 4 MgCl2, 4 M CaCl2, 11 glucose at pH 7.4 with 5% CO2/ 95% O2. Recordings were done at 34ºC. hiPSC-astrocytes were identified based on the td-Tomato fluorescence with a 40x objective in an epifluorescent microscope (Zeiss Axio Examiner.A1). Whole-cell current clamp recordings were made from 17 hiPSC-astrocytes (hiPSC lines #1 to #4, n=6 mice) with borosilicate glass recording pipettes (resistance 3-6MΩ). Pipettes were pulled on a horizontal micropipette puller (Sutter P-1000) and filled with a K-gluconate based internal medium consisting of (mM): 135 K-Gluconate, 4 KCl, 2 NaCl, 10 HEPES, 4 EGTA, 4 MgATP, 0.3 NaATP (pH 7.25). To post-hoc identify the patched astrocyte and analyze its potential to form gap-junctions, 40 µM Alexa Fluor hydrazide dye 488 (Invitrogen) was included in the internal medium. Current steps of incrementing 20 pA were injected starting from 50 pA up to 150 pA. Resting membrane potential was calculated using Clampfit 10.7 (Axon Instruments). Currents were sampled at 20 kHz and stored after 3 kHz low-pass Bessel filtering. The data was low-pass filtered at 1 kHz (Molecular devices DigiData 1440A and Multiclamp 700B). Pipette series

229 resistance and membrane holding current were monitored throughout all recordings to ensure

230 stability of the recording.

231

232 **Immunofluorescence (IF) in Chimeric Mice**

233 For IF analysis, mice were anesthetized with CO2 and perfused with phosphate-buffered saline

234 followed by 4% paraformaldehyde solution. The brain was then removed, post-fixed in the

235 same fixative overnight to 48 hr and cut into 40 μm slices on a Leica VT1000S vibratome. IF

236 on grafted brains was performed as described previously (31) using primary and secondary

237 antibodies (Additional file 1, Table S1). Antigen retrieval was performed by microwave boiling

238 the slides in 10mM tri-Sodium Citrate buffer pH 6.0 (VWR). Aβ plaques were detected by

239 staining with Thioflavin (SIGMA). Briefly, for Thioflavin staining brain sections were incubated

240 with a filtered 0.05% aqueous Thioflavin-S (SIGMA) solution in 50% ethanol for 5 min at RT

241 and rinsed gradually with 70%, 95% ethanol and water. Nuclei staining was performed using

242 a specific anti-human Nuclear Antigen antibody (hNuclei) (Additional file1, Table S1), the pan-

243 nuclear staining TOPRO3 (Invitrogen), or DAPI (SIGMA). The sections were mounted with

244 Glycergel (DAKO). Confocal images were obtained using a Nikon Ti-E inverted microscope

245 equipped with an A1R confocal unit driven by NIS (4.30) software. The confocal was outfitted

246 with 20x (0.75 NA), 40x oil (1.4 NA) and 60x oil (1.4 NA) objectives lenses. For excitation 405

247 nm, 488 nm, 561 nm, 638 nm laser lines were used.

248

249 **Quantification and Statistical Analysis**

250 Morphometry and measurements were performed with Fiji/ImageJ software on animals at five

251 months after transplantation. At least 4-5 different coronal brain sections comprising the

252 transplanted astrocytes and the mouse host tissue were included per animal.

253 Immunofluorescence (IF) sections were imaged by confocal microscopy (Nikon Ti-E inverted

254 microscope) using a 20x (0.75 NA) objective lens to image Z-stacks (8-10 optical sections with

255 a spacing of 1 μm). All images were acquired using identical acquisition parameters as 16-bit,

1024x1024 arrays. Maximum intensity projections and threshold were applied using Fiji/ImageJ to isolate specific fluorescence signals.

For analyses of **cell integration**, brains were sectioned and stained with the antibodies against RFP and hNuclei (human Nuclear antigen). The number of hNuclei+ and RFP+ cells was counted manually on IF images of astrocytes derived from the eight hiPSC lines used on the study (#1 to #8, Table 1). Final counts were corrected for series number (1:6) to get an estimate of the total number of hNuclei+ and RFP+ cells per animal (Additional file 2, Figure S1d).

For analyses of **cell identity**, brains were sectioned and stained with the following antibodies: RFP and hNuclei (human Nuclear antigen), GFAP (astroglia marker), NeuN (neuronal marker) or APC (marker of oligodendrocytes). Results are shown for four hiPSC lines (#1, #2, #7 and #8, Table 1). Total percentages of RFP+ cells co-localizing with GFAP (n=14 mice), hNuclei (n=15 mice), NeuN or APC (n=9 mice each) were manually determined on IF images using Fiji/ImageJ. Data are represented as mean ± SEM. Statistical analyses were done with Student's t test (Fig. 1 and Additional file 3, Figure S2).

To analyze the **morphological subtypes of hiPSC-astrocytes**, brains were sectioned and stained with antibodies against RFP and hNuclei (human Nuclear antigen) and morphometry analyses were manually performed on IF images using Fiji/ImageJ. Results are shown for two hiPSC lines (#1 and #2, Table1) in WT mice (n=9). Data are represented as mean ± SEM (Fig. 3).

For quantification of the average **cell area**, brains were stained with RFP and GFAP, and the NIS-elements software was used (version 5.21.01 build 1483, Nikon Instruments). All the z-stacks were first denoised (denoise.ai tool) and then projected on a 2D image using an extended focus operation (EDF, zero-based, balanced). The resulting 2D image was used for further quantification with a General Analysis (GA3) protocol. In short, to count the number of cells, a spot detection approach was used (average size 11 μm). For detection of the cell area, we first applied a rolling ball filter (6 μm) and, consequently, a thresholding step. Both the settings for the threshold and the spot detection were adjusted per image to compensate for differences in intensity due to a change of acquisition parameters. Results are shown for four

284   hiPSC lines (#1, #2, #3 and #4, Table1) in WT mice (n=12). Data are represented as mean ±

285   SEM. Statistical analysis was done with Student's t test (Fig. 3).

286   To analyze the **morphological responses to Aβ plaques**, brains were sectioned and stained

287   with RFP and Thioflavin and morphometry analyses were manually performed on IF images

288   using Fiji/ImageJ. Results are shown for two hiPSC lines (#1 and #2, Table1) in AD mice (n=7).

289   Data are represented as mean ± SEM. Statistical analysis was performed with Chi-square t

290   test (Fig. 5).

291

292   **Neuropathology on Human Brain Samples**

293   Brain tissue samples from 4 AD, 5 pre-AD and 3 non-demented control patients were included

294   in this study (Table 2). The autopsies were performed with informed consent in accordance

295   with the applicable laws in Belgium (UZ Leuven) and Germany (Ulm, Bonn and Offenbach).

296   The use of human tissue samples for this study was approved by the UZ Leuven ethical

297   committee (Leuven, Belgium). Brain tissues were collected as described in previous studies

298   (42) with an average post-mortem interval (PMI) of 48 h. Briefly, after autopsy, the brains were

299   fixed in 4% aqueous solution of formaldehyde for 2–4 weeks. Samples of the anterior

300   entorhinal cortex and hippocampus were dissected coronally, dehydrated and embedded in

301   paraffin. The paraffin blocks were microtomed at 10 μm, mounted on Flex IHC adhesive

302   microscope slides (Dako), and dried at 55 °C before storing. For neuropathological analysis,

303   sections from all blocks were stained with anti-pTau (AT8), anti-Aβ (4G8) (Additional file 1,

304   Table S1), and with the Gallyas and the Campbell-Switzer silver techniques for detection of

305   neurofibrillary changes and amyloid deposits (43).

306   The post-mortem diagnosis of AD pathology was based upon the standardized clinico-

307   pathological criteria, including the topographical distribution of Aβ plaques in the medial

308   temporal lobe (AβMTL phase) based on Aβ immunohistochemistry (43), and the Braak

309   neurofibrillary tangle (NFT) stage based on pTau immunohistochemistry (44). The study

310   comprised 12 cases with an average age of 77 years and a female to male ratio of 4:8. The

cases were divided in three groups based on the clinical and neuropathological diagnosis: (1)

AD = high-intermediate degree of AD pathology and signs of cognitive decline during life (CDR

≥ 0.5); (2) p-preAD = cases with intermediate-low degrees of AD pathology lacking clinical

signs of cognitive decline (CDR = 0); (3) non-AD = low-no pathological signs of AD pathology

(CDR = 0).

Table 2. Details of Human Cases.

Case number	Age	Gender	Aβ phase	Braak stage	PMI	Neuropathological Diagnosis	Type of dementia
1	82	M	5	3	72	AD	AD
2	81	F	5	5	48	AD, CAA, I	AD
3	85	M	5	3	48	AD, CAA, MI	AD-VaD
4	83	M	5	5	24	AD, CAA, I, B	AD-VaD
5	83	F	4	4	24	p-preAD, AGD, CM	0
6	85	F	4	3	24	p-preAD	0
7	87	M	4	3	96	p-preAD, CAA	0
8	72	M	2	3	72	p-preAD, I	0
9	66	F	0	0	48	non-AD control, AGD	0
10	62	M	0	0	48	non-AD control	0
11	75	M	1	2	48	non-AD control, AGD	0
12	64	M	0	0	24	non-AD control	0

The table shows the human subjects studied for histology of astrocytes. Indicated are: the age

in years, the gender, the Aβ-MTL phase representing the distribution of Aβ deposits in the

subfields of the MTL (43), the stage of neurofibrillary tangle pathology according to Braak and

Braak (44) (NFT stage), PMI, neuropathological diagnosis and type of dementia. F female, M

male, AD Alzheimer's disease, AD-VaD Alzheimer's disease plus signs of vascular dementia,

p-preAD preclinical AD, non-AD non-demented control, AGD argyrophilic grain disease, B

325 bleeding, CAA cerebrovascular angiopathy, CM carcinoma metastasis, I infarction, MI

326 microinfraction, MTL medial temporal lobe, NFT neurofibrillary tangle, PMI post-mortem

327 interval.

328

329 **Immunohistochemistry and Immunofluorescence on Human Samples**

330 The distribution of astrocytes and Aβ deposits was examined in human samples of the

331 entorhinal cortex and hippocampus using immunohistochemical and immunofluorescence

332 techniques. Immunohistochemical detection of Aβ deposits and astrocytes was performed

333 after formic acid pretreatment. For double-labeling, a monoclonal anti-Aβ$_{17-24}$ antibody (4G8,

334 Additional file 1, Table S1) was subsequently combined with a polyclonal anti-GFAP (DAKO,

335 Additional file 1, Table S1) as described previously (43). The anti-Aβ$_{17-24}$ antibody was

336 detected with biotinylated secondary antibodies and ABC, and visualized with

337 3,3′diaminobenzidine-HCl. After peroxidase blocking, the anti-GFAP was applied, detected

338 with biotinylated secondary antibodies, and ABC, and visualized with the Vector peroxidase kit

339 SG (blue staining). Microscopy analysis was performed using a light Leica DM2000 LED

340 microscope (Leica Microsystems) and images were captured with a Leica DFC7000 T camera

341 (Leica Microsystems).

342 For double-labeling immunofluorescence, sections were pre-treated as mentioned above and

343 incubated with formic acid for 3 min, when required. Immunostainings were performed with an

344 antibody cocktail and primary antibodies were detected with species-specific fluorescent-

345 conjugated secondary antibodies (Additional file 1, Table S1). Images were captured via Nikon

346 NIS-Elements software using a Nikon A1R laser scanning confocal system coupled to a Nikon

347 Eclipse Ti inverted microscope (Nikon Instruments, Inc.). Acquired data were further processed

348 using ImageJ software (National Institutes of Health).

349

350 **RESULTS**

Human iPSC-Derived Glial Progenitors Engraft the Mouse Brain and Differentiate into Astrocytes

To generate human-mouse astroglia chimeras, we differentiated human iPSCs (hiPSCs) into glial progenitor cells (hGPCs) *in vitro* (39) (Fig. 1a). After 44 days in culture, td-Tomato expressing hGPCs, which expressed several astroglia markers (Additional file 2, Figure S1b), were xenografted into the brains of newborn mice (Fig. 1a). We used transgenic Tg (Thy1-APPSw,Thy1-PSEN1*L166P) 21Jckr, also called APP/PS1-21 mice (40) crossed with immunodeficient NOD.CB17-Prkdc^scid/J, further called NOD-SCID mice (41), to generate AD mice or wild-type (WT) littermates suitable for grafting experiments (31). We transplanted hiPSC lines from AD patients carrying the *APOE E4/E4* alleles and the corresponding corrected *APOE E3/E3* isogenic lines (Table 1).

Five months after transplantation, immunofluorescence (IF) analysis revealed engraftment of human cells throughout the forebrain (Fig. 1b, Additional file 2, Figure S1c). Human cells were identified based on the expression of the td-Tomato marker RFP and of the human nuclear antigen hNuclei. RFP+ cells infiltrate the cortex, corpus callosum and subcortical areas such as the hippocampus, striatum, thalamus or hypothalamus (Fig. 1c-e). Assessment of the engraftment capacity revealed considerable variation across cell lines (Additional file 2, Figure S1d): we show here examples of robust engraftment, with RFP+ cells both in clusters as well as integrated individually within the mouse brain (Fig. 1b, c), but these results were variable with often lower engraftment capacity at 5 months after transplantation (Additional file 2, Figure S1c, d). Variation was independent of the *APOE* genetic background or the patient (overview in Additional file 2, Figure S1d).

Further analyses revealed that at this stage, human RFP+ cells strongly express the astroglia markers GFAP, S100b, Vimentin and Aquaporin-4 (Fig. 1f-i), the latter largely concentrated at the astrocytic end-feet along the blood vessels (Figure 1i). Staining with human specific GFAP antibody (hGFAP), confirms the human origin of the cells (Additional file 3, Figure S2a). Quantification showed that 93% of the RFP+ hiPSC-cells express the astroglia marker GFAP

378   (Fig. 1j) and 95% of the hNuclei+ hiPSC-cells co-express RFP (Fig. 1k). Thus, the RFP marker

379   is not downregulated, and most of the transplanted cells indeed differentiated into human

380   astroglia. This was further confirmed as no or only minimal expression (less than 3%) of

381   neuronal or oligodendroglial markers was observed in RFP+ cells (Fig. 1l, Additional file 3,

382   Figure S2b, c). No differences were observed between *APOE E4/E4* and *APOE E3/E3* lines

383   (Additional file 3, Figure S2d-f). A subset of RFP+ cells identified by their distinct radial glia-

384   like morphology and not expressing GFAP (Additional file 3, Figure S2g-i) often coexisted with

385   RFP+ cells with more complex structures and expressing main astroglia markers. These cells

386   are likely in a progenitor state which was also described previously (23,45).

387   **Transplanted iPSC-Derived Astrocytes Integrate Functionally Within the Mouse Brain**

388   We assessed morphological and electrophysiological features of individual hiPSC-derived

389   astrocytes in the chimeric brain. We observed hiPSC-astrocytes extending processes that

390   terminated in end-feet contacting mouse host vasculature in the chimeric brains (Fig. 2a)

391   similar to human astrocytes in the human brain (Fig. 2b). Moreover, hiPSC-astrocytes strongly

392   expressed the gap-junction marker Connexin-43 in their processes (Fig. 2c). The gap junctions

393   were functioning, as the Alexa488 dye loaded through the patch clamp pipette on RFP+

394   astrocytes diffused into neighboring mouse host cells (Fig. 2d-h). Electrophysiological

395   analyses on acute brain slices of chimeric mice at 4-5 months showed that transplanted RFP+

396   astrocytes displayed properties resembling human astrocytes (46). Specifically, their non-

397   excitable responses to stimulations with current injection in current clamp mode (Fig. 2i),

398   resting membrane potentials (Fig. 2j), and linear current to voltage (I/V) curves (Fig. 2k).

399   Human iPSC-astrocytes do not replace the endogenous murine astrocytes and both cell types

400   are found in the chimeric mouse brains (Additional file 3, Figure S2j). These data reveal that

401   the transplanted hiPSC-astrocytes are able to integrate functionally within the mouse host

402   brain, show human-like physiological features and co-exist with endogenous mouse

403   counterparts.

Human iPSC-Derived Astrocytes Acquire Human-Specific Morphologies and Features In Vivo

An advantage of low engraftment capacity is that it favors the assessment of morphological details of the transplanted astrocytes. Five months after transplantation, four main morphological subtypes of hiPSC-derived astrocytes were identified in the chimeric brains of the control animals. RFP+ interlaminar astrocytes were frequently observed in superficial layers of the cortex and close to the ventricles, with their small and round cell bodies near the pial surface and their long, unbranched and sometimes tortuous processes descending into deeper layers (Fig. 3a-c). Varicose-projection astrocytes were relatively sparse but easily identified by their bushy appearance and the presence of long processes with regularly spaced beads or varicosities (Fig. 3d, e). Protoplasmic astrocytes were found in deeper layers of the brain and showed the characteristic star-shaped morphology and shorter processes extending in all directions and often contacting the vasculature (Fig. 3f, g). Fibrous astrocytes were found in white matter tracts and presented the typical morphology with small soma and fine, straight and radially oriented processes (Fig. 3h-j). Interlaminar astrocytes were the most abundant subtype of hiPSC-astrocytes in the mouse brain, summing up to 62% of the RFP+ cells, and similar proportions of fibrous and protoplasmic astrocytes were found (16% and 13% of the RFP+ cells respectively). The varicose-projection astrocytes are the less frequent subtype, constituting 9% of RFP+ cells found in the host brain (Fig. 3k). Interestingly, we found the same astroglia subtypes in the human entorhinal cortex and white matter tracts of various control individuals (Table 2, subjects 10-12), when staining with the astrocyte marker GFAP: subpial interlaminar astrocytes with their soma in superficial layers of the cortex (molecular layer to pre-α) and long processes extending into deeper layers (Fig. 4a-c), protoplasmic (Fig. 4a, d) and varicose-projection astrocytes (Fig. 4e-f) in deeper layers of the cortex (pri-α to pri-γ), and fibrous astrocytes in white matter tracts (Fig. 4g-i). Of note, hiPSC-astrocytes covered about 15-fold larger areas than mouse astrocytes and displayed more complex structures (Fig. 3l-m, Additional file 3, Figure S2j). Thus, transplanted hiPSC-astrocytes were able to keep their

431 intrinsic properties and develop in a cell-autonomous way adopting human-specific features

432 and morphologies within the mouse host brain.

433 **Human Astroglia Display Differential Morphological Responses to Amyloid-β Plaques**

434 Interestingly, transplanted hiPSC-astrocytes adopt three clearly distinct morphologies in the

435 brains of chimeric AD mice five months after transplantation, when the Aβ load is high.

436 Immunofluorescence analyses with RFP revealed that about 25% of the astrocytes became

437 hypertrophic and showed thicker processes that surround Aβ deposits (Fig. 5a-c and 5a'-c',

438 Fig. 5g). 62% of the astrocytes seemed not to be morphologically affected at all, even when in

439 close contact with the Aβ plaques (Fig. 5d, 5d', 5g). Finally, about 13% of astrocytes showed

440 atrophic features, displaying thinner processes that sometimes even looked degenerating (Fig.

441 5e-f and 5e'-f', Fig. 5g). *APOE* E3/E3 or *APOE* E4/E4 genotype did not affect these proportions

442 (Fig. 5h). Hypertrophic, atrophic and quiescent phenotypes were also found in human

443 astrocytes in close proximity to Aβ deposits in the entorhinal cortex and hippocampus of

444 patients with AD (Table 2, subjects 1-4), both by immunohistochemistry (Fig. 6) and

445 immunofluorescence (Fig. 7).

446 In conclusion: engrafted hiPSC-astrocytes show differential morphological responses to Aβ

447 plaques that resemble that of human astrocytes in AD patients' brains. The potential of

448 astrocytes to become hyper- or a-trophic, or remain in a quiescent state, does not seem to be

449 influenced by the *APOE* genetic background.

450

451 **DISCUSSION**

452 A major challenge to model astroglia function in AD is the difference between mouse and

453 human astrocytes. A powerful approach to overcome this challenge is the use of hiPSC-

454 derived astrocytes to generate chimeric mice.

455 We investigate in the current study the potential of such experiments using patient derived

456 iPSC lines and isogenic counterparts (Table1). We include AD mice and control littermates.

457 We demonstrate integration of human glia into the mouse brain and differentiation of the

458 majority of cells into four main subtypes of astrocytes expressing main astroglial markers and

459 showing human-specific large, complex morphologies and electrophysiological properties.

460 Additionally, hiPSC-astrocytes contact blood vessels and couple via gap-junctions with mouse

461 cells, demonstrating functional integration in the host brain. In contrast to other glia chimeric

462 models (35), we do not see replacement of the endogenous murine counterparts.

463 hiPSC-astrocytes respond robustly to Aβ pathology showing hypertrophic, atrophic or

464 unaffected morphologies that are very similar to the morphological changes observed in

465 astrocytes in AD patients' brains (15–17). Such responses are not dependent on the *APOE*

466 genetic background. Further work is however needed to understand whether the different

467 *APOE* variants influence the molecular and functional states of human astrocytes surrounding

468 Aβ plaques.

469 While human astrocytes were consistently detected in every injected brain, the number of

470 engrafted cells varied largely from a few hundreds or thousands to >50,000 cells (Additional

471 file 2, Figure S1d). This, combined with the difficulty of recovering the engrafted cells from the

472 mouse brain for single-cell analysis, made further molecular analyses of the cellular

473 phenotypes, unfortunately, not possible at this moment.

474 Others have also observed variations in transplantation efficiencies of hiPSC-derived microglia

475 and neurons (47,48). While many successful reports on "glia" chimeric mice have been

476 reported (23,34–36,49), these glia chimeras develop, in addition to human astrocytes, a large

477 number of human NG2 cells and oligodendrocytes, whose relative ratios varied considerably

478 across different brain regions and animals (23,34,49). This suggests that in these other

479 experiments a different glia precursor state has been transplanted which maintains more 'stem

480 cell like' properties allowing these cells to spread over the brain and to compete with mouse

481 glia as shown before (49). We speculate that in our experimental conditions we have

482 transplanted more differentiated cells which are closer to a final astrocyte phenotype and

483 therefore not able to proliferate once they were injected in the brain of the host mice. It will now

484 be critical to define the optimal window for transplantation of differentiating hiPSCs in order to

485 maximize astrocyte colonization of the mouse brain. In other experiments we succeeded

486 already to determine this for microglia using the Migrate protocol (Fattorelli et al, 2020). In the

487 Migrate protocol there is a very critical window during the cell differentiation *in vitro* that results

488 in 60-80% chimerism. One week longer in culture results in < 5% chimerism although the cells

489 before transplantation look morphologically identical to the more efficiently transplanted ones.

490 Other possible improvements would be the use of RAG2-/- mice which can be maintained for

491 a much longer time period than the NOD-SCID mice we use here.

492

493 **CONCLUSIONS**

494 In conclusion, despite some intrinsic limitations, the approach to transplant human astroglia

495 into mouse brain to study astrocyte pathophysiology in AD is promising. We recapitulated here

496 typical morphological responses of human astrocytes to amyloid plaques *in vivo*. Moreover,

497 the combination of the model with isogenic *APOE* lines points out the potential use of this

498 approach to analyze the impact of patient-derived and genetically modified astroglia on human

499 CNS disease.

500

501 **LIST OF ABBREVIATIONS**

502 5 M: 5 months of age; AD: Alzheimer's disease; Aβ: amyloid-β; APOE: Apolipoprotein E; CDR:

503 clinical dementia rating, DIV: days in vitro; EB: embryoid bodies; GPCs: glia progenitor cells;

504 hiPSCs: human induced pluripotent stem cells; IF: immunofluorescence; IVC: individually

505 ventilated cages; NFT: neurofibrillary tangles; NPCs: neural progenitor cells; PAM: protospacer

506 adjacent motif; PMI: post-mortem interval; RFP: red fluorescent protein; RT: room temperature;

507 SPF: specific pathogen free; ssODN: single-strand oligo-deoxynucleotide; Tzv: Thiazovivin;

508 WT: Wild-type.

509

510 **DECLARATIONS**

543

Authors' contributions

545   AMA and BDS conceived the study and planned experiments. AMA, PP, JTCW, AS, SC, MAT,

546   NC, and SM performed the experiments. All authors interpreted data. AMA and BDS wrote the

547   first version of the manuscript. All authors contributed to and approved the final version.

548

554

REFERENCES

556   1.   Ferrer I (2018) Astrogliopathy in Tauopathies. Neuroglia 1:126–150. doi:

557   10.3390/neuroglia1010010

558   2.   Verkhratsky A, Nedergaard M (2018) Physiology of Astroglia. Physiol Rev 98:239–389.

559   doi: 10.1152/physrev.00042.2016

560   3.   Liddelow SA, Guttenplan KA, Clarke LE, Bennett FC, Bohlen CJ, Schirmer L, Bennett

561   ML, Münch AE, Chung W-S, Peterson TC, Wilton DK, Frouin A, Napier BA, Panicker N, Kumar

562   M, Buckwalter MS, Rowitch DH, Dawson VL, Dawson TM, Stevens B, Barres BA (2017)

563   Neurotoxic reactive astrocytes are induced by activated microglia. Nature 541:481-487. doi:

564   10.1038/nature21029

565   4.   Ouali Alami N, Schurr C, Olde Heuvel F, Tang L, Li Q, Tasdogan A, Kimbara A,

566   Nettekoven M, Ottaviani G, Raposo C, Röver S, Rogers-Evans M, Rothenhäusler B, Ullmer C,

567   Fingerle J, Grether U, Knuesel I, Boeckers TM, Ludolph A, Wirth T, Roselli F, Baumann B

568   (2018) NF-κB activation in astrocytes drives a stage-specific beneficial neuroimmunological

569   response in ALS. EMBO J. 37:e98697. doi: 10.15252/embj.201798697

570   5.   Rothhammer V, Borucki DM, Tjon EC, Takenaka MC, Chao C, Ardura-fabregat A, Lima

571   KA De, Gutiérrez-vázquez C, Hewson P, Staszewski O, Blain M, Healy L, Neziraj T, Borio M,

572   Wheeler M, Dragin LL, Laplaud DA, Antel J, Alvarez JI, Prinz M, Quintana FJ (2018) Microglial

573   control of astrocytes in response to microbial metabolites. Nature 557:724-728. doi:

574   10.1038/s41586-018-0119-x

575   6.   Yun SP, Kam T, Panicker N, Kim S, Oh Y, Park J, Kwon S, Park YJ, Karuppagounder

576   SS, Park H, Kim S, Oh N, Kim NA, Lee S, Brahmachari S, Mao X, Lee JH, Kumar M, An D,

577   Kang S, Lee Y, Lee KC, Na DH, Kim D, Lee SH, Roschke V V, Liddelow SA, Mari Z, Barres

578   BA, Dawson VL, Lee S (2018) Block of A1 astrocyte conversion by microglia is neuroprotective

579   in models of Parkinson ' s disease. Nat Med. 24:931-938. doi: 10.1038/s41591-018-0051-5

580   7.   Wheeler MA, Clark IC, Tjon EC, Li Z, Zandee SEJ, Couturier CP, Watson BR, Scalisi

581   G, Alkwai S, Rothhammer V, Rotem A, Heyman JA, Thaploo S, Sanmarco LM, Ragoussis J,

582   Weitz DA, Petrecca K, Moffitt JR, Becher B, Antel JP, Prat A, Quintana FJ (2020) MAFG-driven

583   astrocytes promote CNS inflammation. Nature 578:593–599. doi: 10.1038/s41586-020-1999-

584   0

585   8.   Arranz AM, De Strooper B (2019) The role of astroglia in Alzheimer's disease:

586   pathophysiology and clinical implications. Lancet Neurol 18:406–414. doi: 10.1016/S1474-

587   4422(18)30490-3

588   9.   Lambert JC, Ibrahim-Verbaas CA, Harold D, Naj AC, Sims R, Bellenguez C, et al.

589   (2013) Meta-analysis of 74,046 individuals identifies 11 new susceptibility loci for Alzheimer's

590   disease. Nat Genet 45:1452–8. doi: 10.1038/ng.2802

591   10.   Verheijen J, Sleegers K (2018) Understanding Alzheimer Disease at the Interface

592   between Genetics and Transcriptomics. Trends Genet 34:434–447. doi:

593   10.1016/j.tig.2018.02.007

594   11.   Zhang Y, Sloan SA, Clarke LE, Caneda C, Plaza CA, Blumenthal PD, Vogel H,

595   Steinberg GK, Edwards MSB, Li G, Duncan JA, Cheshier SH, Shuer LM, Chang EF, Grant

596   GA, Gephart MGH, Barres BA (2016) Purification and Characterization of Progenitor and

597   Mature Human Astrocytes Reveals Transcriptional and Functional Differences with Mouse.

598   Neuron 89:37-53. doi: 10.1016/j.neuron.2015.11.013

599   12.   Thal DR, Schultz C, Dehghani F, Yamaguchi H, Braak H, Braak E (2000) Amyloid β-

600   protein (Aβ)-containing astrocytes are located preferentially near N-terminal-truncated Aβ

601   deposits in the human entorhinal cortex. Acta Neuropathol 100:608–617. doi:

602   10.1007/s004010000242

603   13.   Thal DR (2012) The role of astrocytes in amyloid β-protein toxicity and clearance. Exp

604   Neurol 236:1–5. doi: 10.1016/j.expneurol.2012.04.021

605   14.   Mulder SD, Veerhuis R, Blankenstein MA, Nielsen HM (2012) The effect of amyloid

606   associated proteins on the expression of genes involved in amyloid-β clearance by adult

607   human astrocytes. Exp Neurol 233:373–379. doi: 10.1016/j.expneurol.2011.11.001

608   15.   Pike CJ, Cummings BJ, Cotman CW (1995) Early association of reactive astrocytes

609   with senile plaques in Alzheimer's disease. Exp Neurol 132:172–179. doi: 10.1016/0014-

610   4886(95)90022-5

611   16.   Colombo JA, Quinn B, Puissant V (2002) Disruption of astroglial interlaminar processes

612   in Alzheimer's disease. Brain Res Bull 58:235–242. doi: 10.1016/S0361-9230(02)00785-2

613   17.   Hsu ET, Gangolli M, Su S, Holleran L, Stein TD, Alvarez VE (2018) Astrocytic

614   degeneration in chronic traumatic encephalopathy. Acta Neuropathol. 136:955-972. doi:

615   10.1007/s00401-018-1902-3

616   18.   Orre M, Kamphuis W, Osborn LM, Jansen AHP, Kooijman L, Bossers K, Hol EM (2014)

617   Isolation of glia from Alzheimer's mice reveals inflammation and dysfunction. Neurobiol Aging.

618   35:2746-2760. doi: 10.1016/j.neurobiolaging.2014.06.004

619   19.   Lian H, Yang L, Cole A, Sun L, Chiang ACA, Fowler SW, Shim DJ, Rodriguez-Rivera

620   J, Taglialatela G, Jankowsky JL, Lu HC, Zheng H (2015) NFκB-Activated Astroglial Release

621   of Complement C3 Compromises Neuronal Morphology and Function Associated with

622   Alzheimer's Disease. Neuron 85:101-115. doi: 10.1016/j.neuron.2014.11.018

623   20.   Lian H, Litvinchuk A, Chiang AC-A, Aithmitti N, Jankowsky JL, Zheng H (2016)

624   Astrocyte-Microglia Cross Talk through Complement Activation Modulates Amyloid Pathology

625   in Mouse Models of Alzheimer's Disease. J Neurosci 36:577–589. doi:

626   10.1523/JNEUROSCI.2117-15.2016

627   21.   Diniz LP, Tortelli V, Matias XI, Morgado J, Be AP, Melo XHM, Seixas XGS, Alves-leon

628   XS V, Souza XJM De, Ferreira XST, Felice XFG De, Gomes A (2017) Astrocyte Transforming

629   Growth Factor Beta 1 Protects Synapses against Aβ Oligomers in Alzheimer's Disease Model.

630   Journal of Neuroscience 37:6797–6809. doi: 10.1523/JNEUROSCI.3351-16.2017

631   22.   Oberheim NA, Takano T, Han X, He W, Lin JHC, Wang F, Xu Q, Wyatt JD, Pilcher W,

632   Ojemann JG, Ransom BR, Goldman SA, Nedergaard M (2009) Uniquely Hominid Features of

633   Adult Human Astrocytes. J Neurosci. 29:3276-87. doi: 10.1523/JNEUROSCI.4707-08.2009

634   23.   Han X, Chen M, Wang F, Windrem M, Wang S, Shanz S, Xu Q, Oberheim NA, Bekar

635   L, Betstadt S, Silva AJ, Takano T, Goldman SA, Nedergaard M (2013) Forebrain engraftment

636   by human glial progenitor cells enhances synaptic plasticity and learning in adult mice. Cell

637   Stem Cell 12(3):342–53. doi: 10.1016/j.stem.2012.12.015

638   24.   Tarassishin L, Suh HS, Lee SC (2014) LPS and IL-1 differentially activate mouse and

639   human astrocytes: Role of CD14. Glia 62:999–1013. doi: 10.1002/glia.22657

640 25. Lundin A, Delsing L, Clausen M, Ricchiuto P, Sanchez J, Sabirsh A, Ding M,

641 Synnergren J, Zetterberg H, Brolén G, Hicks R, Herland A, Falk A (2018) Human iPS-Derived

642 Astroglia from a Stable Neural Precursor State Show Improved Functionality Compared with

643 Conventional Astrocytic Models. Stem Cell Reports 10:1030–1045. doi:

644 10.1016/j.stemcr.2018.01.021

645 26. Zhao J, Davis MD, Martens YA, Shinohara M, Graff-radford NR, Younkin SG, Wszolek

646 ZK, Kanekiyo T, Bu G (2017) APOE e 4 / e 4 diminishes neurotrophic function of human iPSC-

647 derived astrocytes. Hum. Mol. Genetics. 26:2690–2700. doi: 10.1093/hmg/ddx155

648 27. Oksanen M, Petersen AJ, Naumenko N, Puttonen K, Lehtonen Š, Gubert Olivé M,

649 Shakirzyanova A, Leskelä S, Sarajärvi T, Viitanen M, Rinne JO, Hiltunen M, Haapasalo A,

650 Giniatullin R, Tavi P, Zhang SC, Kanninen KM, Hämäläinen RH, Koistinaho J (2017) PSEN1

651 Mutant iPSC-Derived Model Reveals Severe Astrocyte Pathology in Alzheimer's Disease.

652 Stem Cell Reports 9:1885–1897. doi: 10.1016/j.stemcr.2017.10.016

653 28. Lin YT, Seo J, Gao F, Feldman HM, Wen HL, Penney J, Cam HP, Gjoneska E, Raja

654 WK, Cheng J, Rueda R, Kritskiy O, Abdurrob F, Peng Z, Milo B, Yu CJ, Elmsaouri S, Dey D,

655 Ko T, Yankner BA, Tsai LH (2018) APOE4 Causes Widespread Molecular and Cellular

656 Alterations Associated with Alzheimer's Disease Phenotypes in Human iPSC-Derived Brain

657 Cell Types. Neuron 98:1141-1154.e7. doi: 10.1016/j.neuron.2018.05.008

658 29. TCW J, Liang SA, Qian L, Pipalia NH, Chao MJ, Bertelsen SE, Kapoor M, Marcora E,

659 Sikora E, Holtzman D, Maxfield FR, Zhang B, Wang M, Poon WW, Goate AM (2019)

660 Cholesterol and Matrisome Pathways Dysregulated in Human APOE ∈4 Glia. bioRxiv. 713362.

661 doi: 10.2139/ssrn.3435267

662 30. Perriot S, Mathias A, Perriard G, Canales M, Jonkmans N, Merienne N, Meunier C, El

663 Kassar L, Perrier AL, Laplaud DA, Schluep M, Déglon N, Du Pasquier R (2018) Human

664 Induced Pluripotent Stem Cell-Derived Astrocytes Are Differentially Activated by Multiple

Sclerosis-Associated Cytokines. Stem Cell Reports 11:1199–1210. doi: 10.1016/j.stemcr.2018.09.015

31. Espuny-Camacho I, Arranz AM, Fiers M, Snellinx A, Ando K, Munck S, Bonnefont J, Lambot L, Corthout N, Omodho L, Vanden Eynden E, Radaelli E, Tesseur I, Wray S, Ebneth A, Hardy J, Leroy K, Brion JP, Vanderhaeghen P, De Strooper B (2017) Hallmarks of Alzheimer's Disease in Stem-Cell-Derived Human Neurons Transplanted into Mouse Brain. Neuron 93:1066–1081.e8. doi: 10.1016/j.neuron.2017.02.001

32. Mancuso R, Van Den Daele J, Fattorelli N, Wolfs L, Balusu S, Burton O, Liston A, Sierksma A, Fourne Y, Poovathingal S, Arranz-Mendiguren A, Sala Frigerio C, Claes C, Serneels L, Theys T, Perry VH, Verfaillie C, Fiers M, De Strooper B (2019) Stem-cell-derived human microglia transplanted in mouse brain to study human disease. Nat Neurosci. 22:2111-2116. doi: 10.1038/s41593-019-0525-x

33. Hasselmann J, Coburn MA, England W, Figueroa Velez DX, Kiani Shabestari S, Tu CH, McQuade A, Kolahdouzan M, Echeverria K, Claes C, Nakayama T, Azevedo R, Coufal NG, Han CZ, Cummings BJ, Davtyan H, Glass CK, Healy LM, Gandhi SP, Spitale RC, Blurton-Jones M (2019) Development of a Chimeric Model to Study and Manipulate Human Microglia In Vivo. Neuron 103:1016–1033.e10. doi: 10.1016/j.neuron.2019.07.002

34. Benraiss A, Wang S, Herrlinger S, Li X, Chandler-Militello D, Mauceri J, Burm HB, Toner M, Osipovitch M, Jim Xu Q, Ding F, Wang F, Kang N, Kang J, Curtin PC, Brunner D, Windrem MS, Munoz-Sanjuan I, Nedergaard M, Goldman SA (2016) Human glia can both induce and rescue aspects of disease phenotype in Huntington disease. Nat Commun. 7:11758. doi: 10.1038/ncomms11758

35. Windrem MS, Schanz SJ, Guo M, Tian GF, Washco V, Stanwood N, Rasband M, Roy NS, Nedergaard M, Havton LA, Wang S, Goldman SA (2008) Neonatal Chimerization with Human Glial Progenitor Cells Can Both Remyelinate and Rescue the Otherwise Lethally Hypomyelinated Shiverer Mouse. Cell Stem Cell. 2:553-565. doi: 10.1016/j.stem.2008.03.020

691 36. Windrem MS, Osipovitch M, Liu Z, Bates J, Chandler-Militello D, Zou L, Munir J, Schanz

692 S, McCoy K, Miller RH, Wang S, Nedergaard M, Findling RL, Tesar PJ, Goldman SA (2017)

693 Human iPSC Glial Mouse Chimeras Reveal Glial Contributions to Schizophrenia. Cell Stem

694 Cell 21:195–208.e6. doi: 10.1016/j.stem.2017.06.012

695 37. Paquet D, Kwart D, Chen A, Sproul A, Jacob S, Teo S, Olsen KM, Gregg A, Noggle S,

696 Tessier-Lavigne M (2016) Efficient introduction of specific homozygous and heterozygous

697 mutations using CRISPR/Cas9. Nature 533:125–129. doi: 10.1038/nature17664

698 38. Bowles KR, Julia TCW, Qian L, Jadow BM, Goate AM (2019) Reduced variability of

699 neural progenitor cells and improved purity of neuronal cultures using magnetic activated cell

700 sorting. PLoS One 14:1–18. doi: 10.1371/journal.pone.0213374

701 39. TCW J, Wang M, Pimenova AA, Bowles KR, Hartley BJ, Lacin E, Machlovi SI, Abdelaal

702 R, Karch CM, Phatnani H, Slesinger PA, Zhang B, Goate AM, Brennand KJ (2017) An Efficient

703 Platform for Astrocyte Differentiation from Human Induced Pluripotent Stem Cells. Stem Cell

704 Reports 9:600–614. doi: 10.1016/j.stemcr.2017.06.018

705 40. Radde R, Bolmont T, Kaeser SA, Coomaraswamy J, Lindau D, Stoltze L, Calhoun ME,

706 Jäggi F, Wolburg H, Gengler S, Haass C, Ghetti B, Czech C, Hölscher C, Mathews PM, Jucker

707 M (2006) Abeta42-driven cerebral amyloidosis in transgenic mice reveals early and robust

708 pathology. EMBO Rep 7:940–6. doi: 10.1038/sj.embor.7400784

709 41. Shultz LD, Schweitzer PA, Christianson SW, Gott B, Schweitzer IB, Tennent B,

710 McKenna S, Mobraaten L, Rajan T V, Greiner DL (1995) Multiple defects in innate and adaptive

711 immunologic function in NOD/LtSz-scid mice. J Immunol 154:180–91

712 42. Koper MJ, Van Schoor E, Ospitalieri S, Vandenberghe R, Vandenbulcke M, von Arnim

713 CAF, Tousseyn T, Balusu S, De Strooper B, Thal DR (2020) Necrosome complex detected in

714 granulovacuolar degeneration is associated with neuronal loss in Alzheimer's disease. Acta

715 Neuropathol 139:463–484. doi: 10.1007/s00401-019-02103-y

716 43. Thal DR, Rüb U, Schultz C, Sassin I, Ghebremedhin E, Del Tredici K, Braak E, Braak

717 H (2000) Sequence of Aβ-protein deposition in the human medial temporal lobe. J Neuropathol

718 Exp Neurol 59:733–748. doi: 10.1093/jnen/59.8.733

719 44. Braak H, Alafuzoff I, Arzberger T, Kretzschmar H, Tredici K (2006) Staging of Alzheimer

720 disease-associated neurofibrillary pathology using paraffin sections and

721 immunocytochemistry. Acta Neuropathol 112:389–404. doi: 10.1007/s00401-006-0127-z

722 45. Chen H, Qian K, Chen W, Hu B, Blackbourn LW, Du Z, Ma L, Liu H, Knobel KM, Ayala

723 M, Zhang SC (2015) Human-derived neural progenitors functionally replace astrocytes in adult

724 mice. J Clin Invest 125:1033–1042. doi: 10.1172/JCI69097

725 46. Sosunov AA, Wu X, Tsankova NM, Guilfoyle E, McKhann GM, Goldman JE (2014)

726 Phenotypic heterogeneity and plasticity of isocortical and hippocampal astrocytes in the human

727 brain. J Neurosci 34:2285–2298. doi: 10.1523/JNEUROSCI.4037-13.2014

728 47. Xu R, Li X, Boreland AJ, Posyton A, Kwan K, Hart RP, Jiang P (2020) Human iPSC-

729 derived mature microglia retain their identity and functionally integrate in the chimeric mouse

730 brain. Nat Commun 11: 1577. doi: 10.1038/s41467-020-15411-9

731 48. Kirkeby A, Nolbrant S, Tiklova K, Heuer A, Kee N, Cardoso T, Ottosson DR, Lelos MJ,

732 Rifes P, Dunnett SB, Grealish S, Perlmann T, Parmar M (2017) Predictive Markers Guide

733 Differentiation to Improve Graft Outcome in Clinical Translation of hESC-Based Therapy for

734 Parkinson's Disease. Cell Stem Cell 20:135–148. doi: 10.1016/j.stem.2016.09.004

735 49. Windrem MS, Schanz SJ, Morrow C, Munir J, Chandler-Militello D, Wang S, Goldman

736 SA (2014) A Competitive Advantage by Neonatally Engrafted Human Glial Progenitors Yields

737 Mice Whose Brains Are Chimeric for Human Glia. J Neurosci. 34:16153–16161. doi:

738 10.1523/JNEUROSCI.1510-14.2014

739

740

TABLES AND FIGURE LEGENDS

Table 1. Information on the hiPSC lines. The table shows hiPSC name, patient ethnicity, gender, age of onset, age at skin biopsy, disease status (CDR at biopsy), original *APOE* genotype and genetic modification. F female, M male, AD Alzheimer's disease, APOE apolipoprotein, CDR clinical dementia rating, hiPSC human induced pluripotent stem cells. These cells were previously generated and characterized by [37].

Table 2. Details of the Human Cohort. The table shows the human subjects studied for histology of astrocytes. Indicated are: the age in years, the gender, the Aβ-MTL phase representing the distribution of Aβ deposits in the subfields of the MTL (43), the stage of neurofibrillary tangle pathology according to Braak and Braak (44) (NFT stage), PMI, neuropathological diagnosis and type of dementia. F female, M male, AD Alzheimer's disease, AD-VaD Alzheimer's disease plus signs of vascular dementia, p-preAD preclinical AD, non-AD non-demented control, AGD argyrophilic grain disease, B bleeding, CAA cerebrovascular angiopathy, CM carcinoma metastasis, I infarction, MI microinfraction, MTL medial temporal lobe, NFT neurofibrillary tangle, PMI post-mortem interval.

Fig. 1 hiPSC-glia progenitors engraft the mouse brain and differentiate into astrocytes.
(a) Schematics of the differentiation and transplantation procedures. hiPSCs: human induced pluripotent stem cells, NPCs: neural progenitor cells, GPCs: glia progenitor cells, SB: SB431542, LDN: LDN193189, FGF2: fibroblast growth factor 2, AGS: astrocyte growth supplement. Scale bars: 100 µm. **(b)** RFP staining (red) shows the distribution of hiPSC-derived astrocytes on a coronal brain section of a chimeric mouse at five months after transplantation. Scale bar: 200 µm. **(c)** Dot map displaying the widespread distribution of the hiPSC-derived astrocytes (RFP, red) in four coronal sections of this mouse brain. **(d-e)** RFP (red) and hNuclei (green) expressing hiPSC-astrocytes depict a complex fine structure in the cortex (CTX) and corpus callosum (CC) of chimeric mice. Scale bars: 50 µm (d), 25 µm (e). **(d'-e')** Enlarged images of the inserts in d and e. **(f-i)** Engrafted hiPSC-astrocytes (RFP+, red) express GFAP (f), S100b (g), Vimentin (h) and AQP4 (i) (green) five months after

768 transplantation. Scale bars: 25 μm. **(j)** Percentage of RFP+ cells expressing GFAP (n=14

769 mice). **(k)** Percentage of hNuclei+ cells expressing RFP (n=15 mice). **(l)** Percentage of RFP+

770 cells expressing NeuN and APC (n=9 mice). Data are represented as mean ± SEM

771 **Fig. 2 hiPSC-astrocytes integrate functionally within the mouse brain. (a-b)** A xenografted

772 hiPSC-astrocyte in the chimeric mouse brain (a, red) and a GFAP+ cortical astrocyte in the

773 human brain (b, brown) contacting blood vessels with their end-feet. Scale bars: 25 μm. **(c)**

774 hiPSC-astrocyte processes (RFP, red) express the gap junction marker Cx43 (green, arrows).

775 Scale bar: 2 μm. **(d)** The gap-junction dye Alexa488 loaded on a hiPSC-astrocyte (RFP+, red)

776 diffuses into RFP- neighboring host cells. Scale bar: 25 μm. **(e-h)** Enlarged views of the area

777 selected in d. (e) RFP+ hiPSC-astrocyte, (f) Alexa488 dye, (g) Nuclei stained with DAPI, (h)

778 Overlay. Arrows point to Alexa488+ RFP- host cells. **(i-k)** Representative traces of current

779 injection steps of 20mV (i), resting membrane potentials (j) and current-voltage (I/V) curves (k)

780 of hiPSC-astrocytes in the host brain (n=17 cells from 6 mice). Data are represented as mean

781 ± SEM

782 **Fig. 3 hiPSC-astrocytes recapitulate human morphological subtypes and retain human**

783 **specific features within the mouse brain. (a-j)** Representative images of RFP+ (white)

784 interlaminar (a-c), varicose-projection (d-e), protoplasmic (f-g) and fibrous astrocytes (h-j) in

785 the brain of wild-type mice five months after transplantation. Scale bars: 25 μm. **(k)** Histogram

786 showing the percentage of RFP+ cells of each astroglial subtype on the mouse brain (n=9

787 mice). Data are represented as mean ± SEM. **(l)** Representative image showing mouse (green,

788 arrows) and hiPSC-astrocytes (red) on a chimeric mouse brain five months after

789 transplantation. Scale bar: 25 μm. **(m)** Histogram plotting the size of hiPSC-derived astrocytes

790 vs mouse astrocytes on the host brain (n=12 mice). Data are represented as mean ± SEM,

791 Student's t test: ****p<0.0001

792 **Fig. 4 Four subtypes of morphologically defined GFAP+ astrocytes in the human**

793 **entorhinal cortex and white matter. (a)** Overview of human entorhinal cortex layers stained

794 with GFAP (brown) to detect astrocytes. Layers molecular to lamina dissecans are mainly

31

composed of subpial interlaminar astrocytes, while layers pri-α to pri-γ are rich in protoplasmic astrocytes (arrows). **(b-f)** Representative images of subpial interlaminar astrocytes (b) and their tortuous processes (c), protoplasmic astrocytes (d), varicose-projection astrocytes (e) and their beaded processes (f). **(g-i)** Overview of human white matter (g) and GFAP+ fibrous astrocytes (h-i). mol: molecular layer, diss: lamina dissecans. Scale bars: 50 µm in (a) and (g); 25 µm in (b) and (h); 10 µm in (c-f) and (i)

Fig. 5 hiPSC-astrocytes show differential morphological responses to Aβ plaques within the chimeric mouse brain. (a-f, a'-f') hiPSC-astrocytes (RFP+, red) exposed to Aβ plaques (Thioflavin, green) show hypertrophic (a-c, a'-c'), quiescent (d, d') and atrophic (e-f, e'-f') morphologies in AD chimeric mice five months after transplantation. Scale bars: 25 µm. **(g-h)** Percentage of hiPSC-astrocytes showing differential morphologies as a group (g, n=7 mice) and per ApoE genotype (h, n=3 mice for APOE3/3; n=4 mice for APOE4/4) five months post-transplantation. Data are represented as mean ± SEM, Chi-square test: n.s., non-significant

Fig. 6 Astrocytes display differential responses to Aβ in the human AD-patient brain. (a-f) Representative immunohistochemistry images of GFAP+ astrocytes (brown) around amyloid-deposits (blue, dashed lines) in the cortex and hippocampus of AD-patient brains. **(a-d)** Overviews (a, b) and enlarged views (c, d) of the insets in a, b respectively. **(c-f)** GFAP+ hypertrophic (red arrows) and quiescent or atrophic (green arrows) astrocytes around amyloid-deposits. Scale bars: 25 µm in (a, b); 10 µm in (c-f)

Fig. 7 Hypertrophic, quiescent and atrophic astrocytes close to amyloid deposits in the human AD-patient brain. (a-l) Representative immunofluorescence images of GFAP+ astrocytes (red) around amyloid-deposits (4G8, green) in the cortex and hippocampus of AD patient brains. **(c-l)** GFAP+ astrocytes (red) show hypertrophic (d-e, i-j), quiescent (f, k) and atrophic (g, l) morphologies close to amyloid deposits. (d-g, i-l) Enlarged views of the insets in c and h respectively. Scale bars: 50 µm in (a, b) and 25 µm in (c, h)

Figures

Figure 1

hiPSC-glia progenitors engraft the mouse brain and differentiate into astrocytes. (a) Schematics of the differentiation and transplantation procedures. hiPSCs: human induced pluripotent stem cells, NPCs: neural progenitor cells, GPCs: glia progenitor cells, SB: SB431542, LDN: LDN193189, FGF2: fibroblast

growth factor 2, AGS: astrocyte growth supplement. Scale bars: 100 μm. (b) RFP staining (red) shows the distribution of hiPSC- derived astrocytes on a coronal brain section of a chimeric mouse at five months after transplantation. Scale bar: 200 μm. (c) Dot map displaying the widespread distribution of the hiPSC-derived astrocytes (RFP, red) in four coronal sections of this mouse brain. (d-e) RFP (red) and hNuclei (green) expressing hiPSC-astrocytes depict a complex fine structure in the cortex (CTX) and corpus callosum (CC) of chimeric mice. Scale bars: 50 μm (d), 25 μm (e). (d'-e') Enlarged images of the inserts in d and e. (f-i) Engrafted hiPSC-astrocytes (RFP+, red) express GFAP (f), S100b (g), Vimentin (h) and AQP4 (i) (green) five months after 31 transplantation. Scale bars: 25 μm. (j) Percentage of RFP+ cells expressing GFAP (n=14 mice). (k) Percentage of hNuclei+ cells expressing RFP (n=15 mice). (l) Percentage of RFP+ cells expressing NeuN and APC (n=9 mice). Data are represented as mean ± SEM
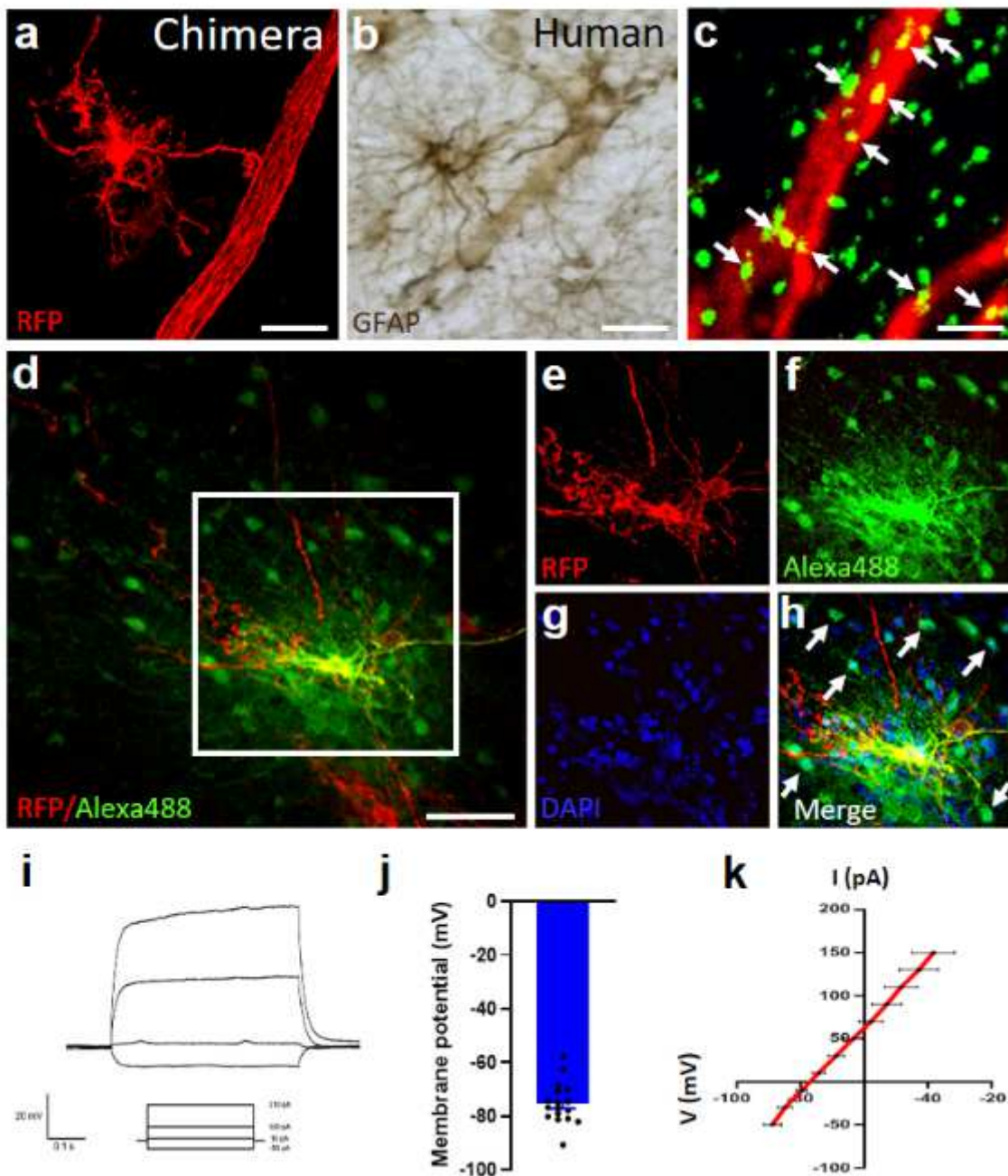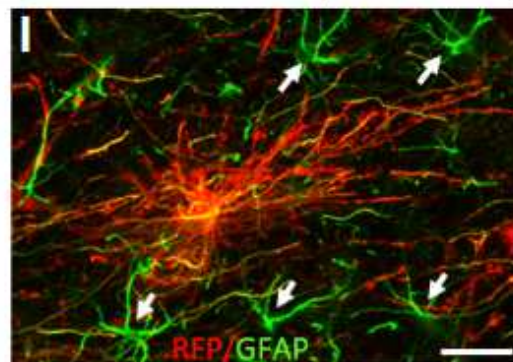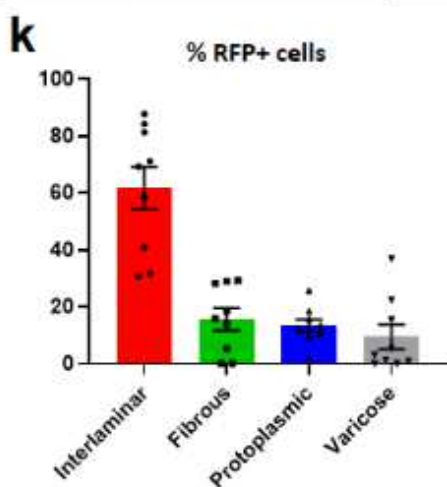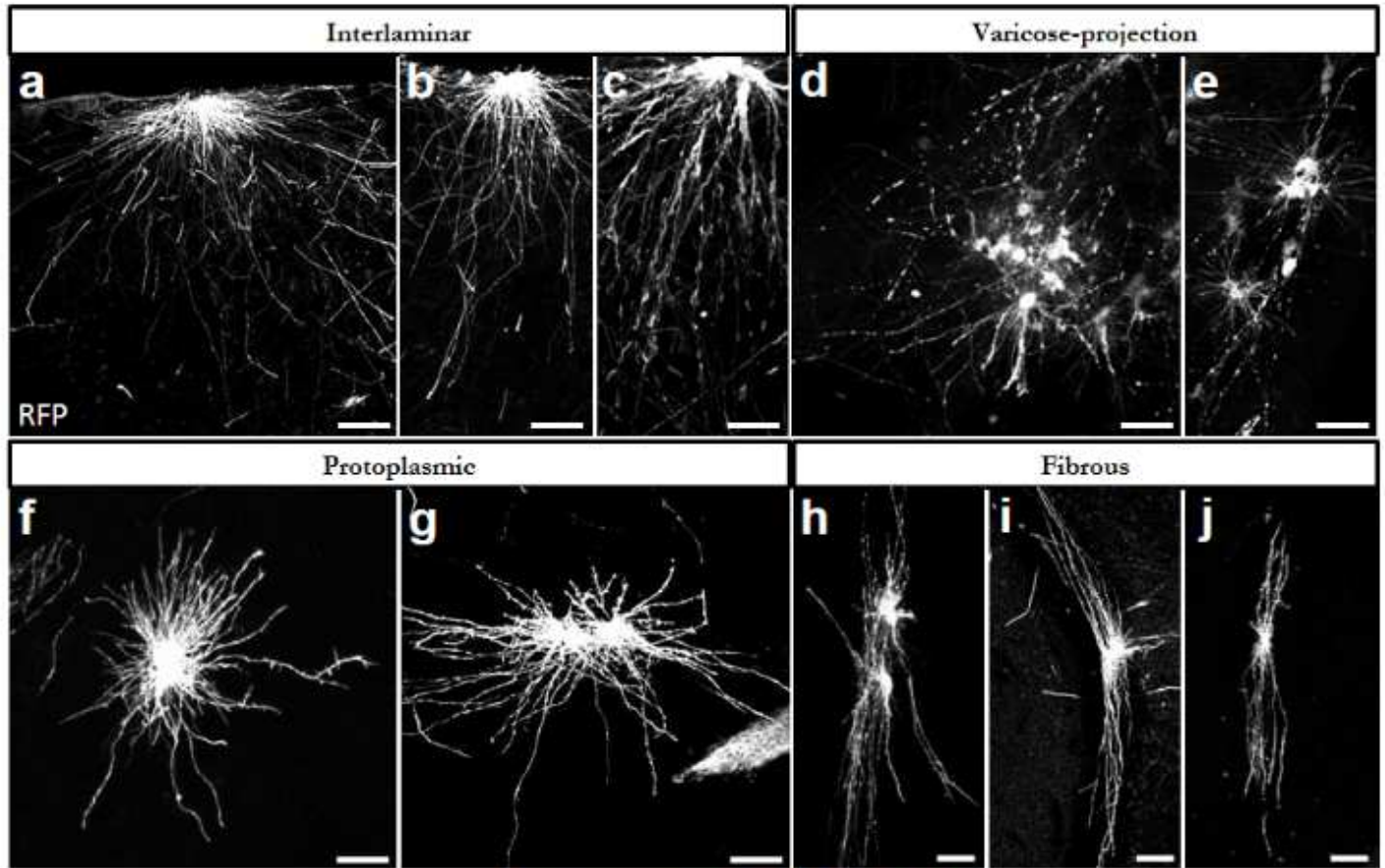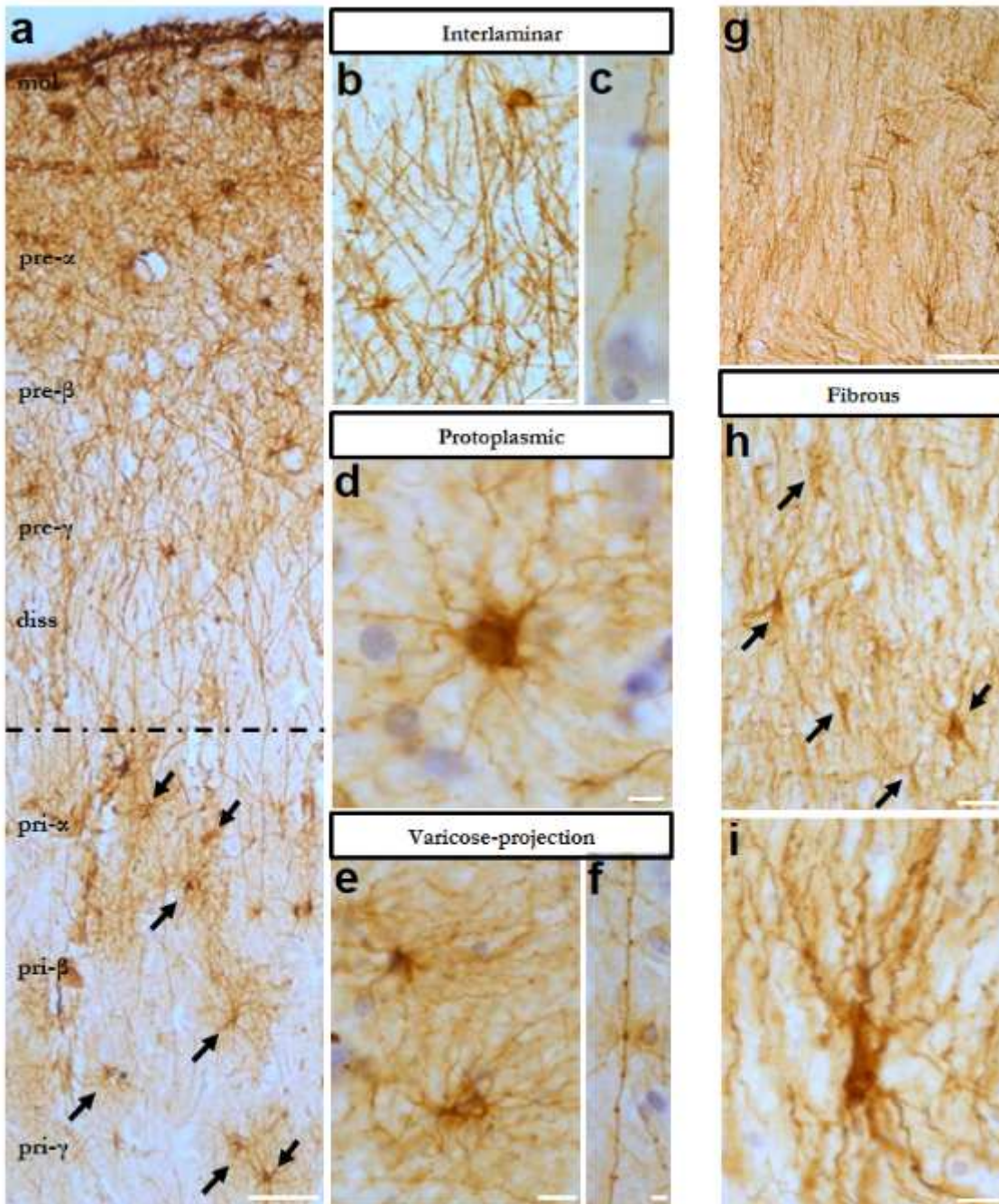

Figure 2

hiPSC-astrocytes integrate functionally within the mouse brain. (a-b) A xenografted hiPSC-astrocyte in the chimeric mouse brain (a, red) and a GFAP+ cortical astrocyte in the human brain (b, brown) contacting blood vessels with their end-feet. Scale bars: 25 μm. (c) hiPSC-astrocyte processes (RFP, red) express the gap junction marker Cx43 (green, arrows). Scale bar: 2 μm. (d) The gap-junction dye Alexa488 loaded on a hiPSC-astrocyte (RFP+, red) diffuses into RFP- neighboring host cells. Scale bar: 25 μm. (e-h) Enlarged views of the area selected in d. (e) RFP+ hiPSC-astrocyte, (f) Alexa488 dye, (g) Nuclei stained with DAPI, (h) Overlay. Arrows point to Alexa488+ RFP- host cells. (i-k) Representative traces of current injection steps of 20mV (i), resting membrane potentials (j) and current-voltage (I/V) curves (k) of hiPSC-astrocytes in the host brain (n=17 cells from 6 mice). Data are represented as mean ± SEM
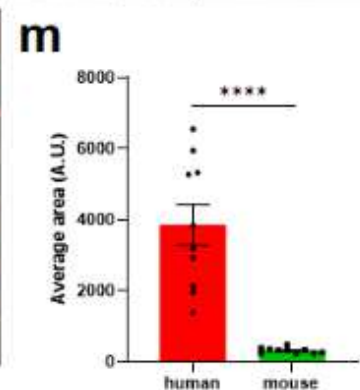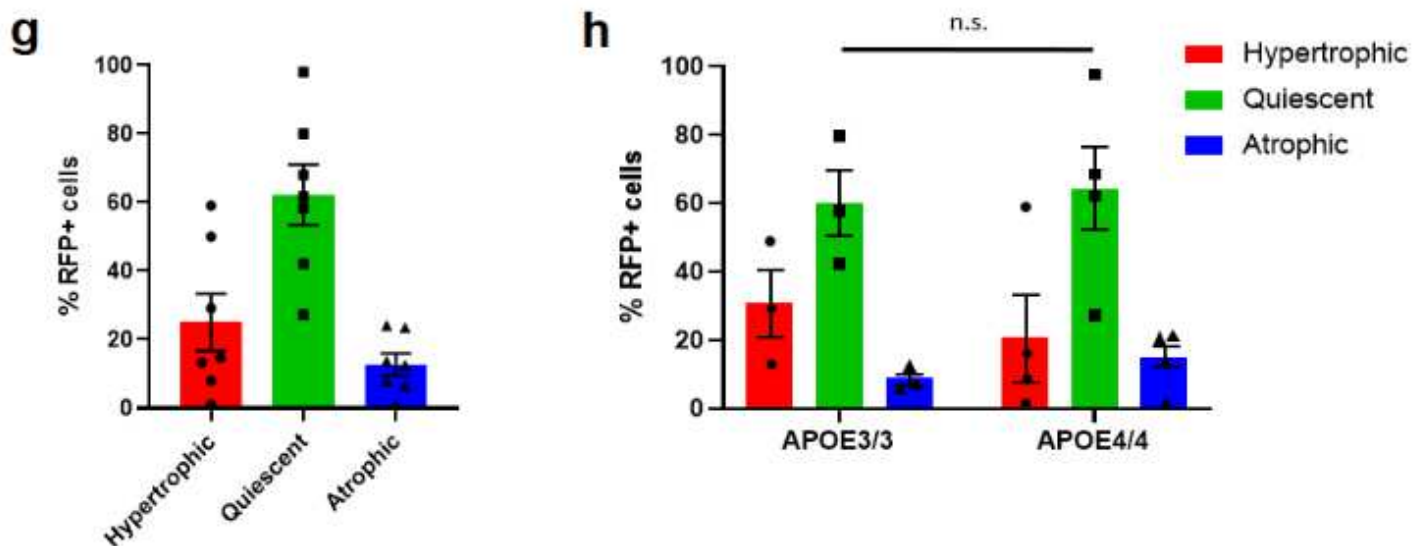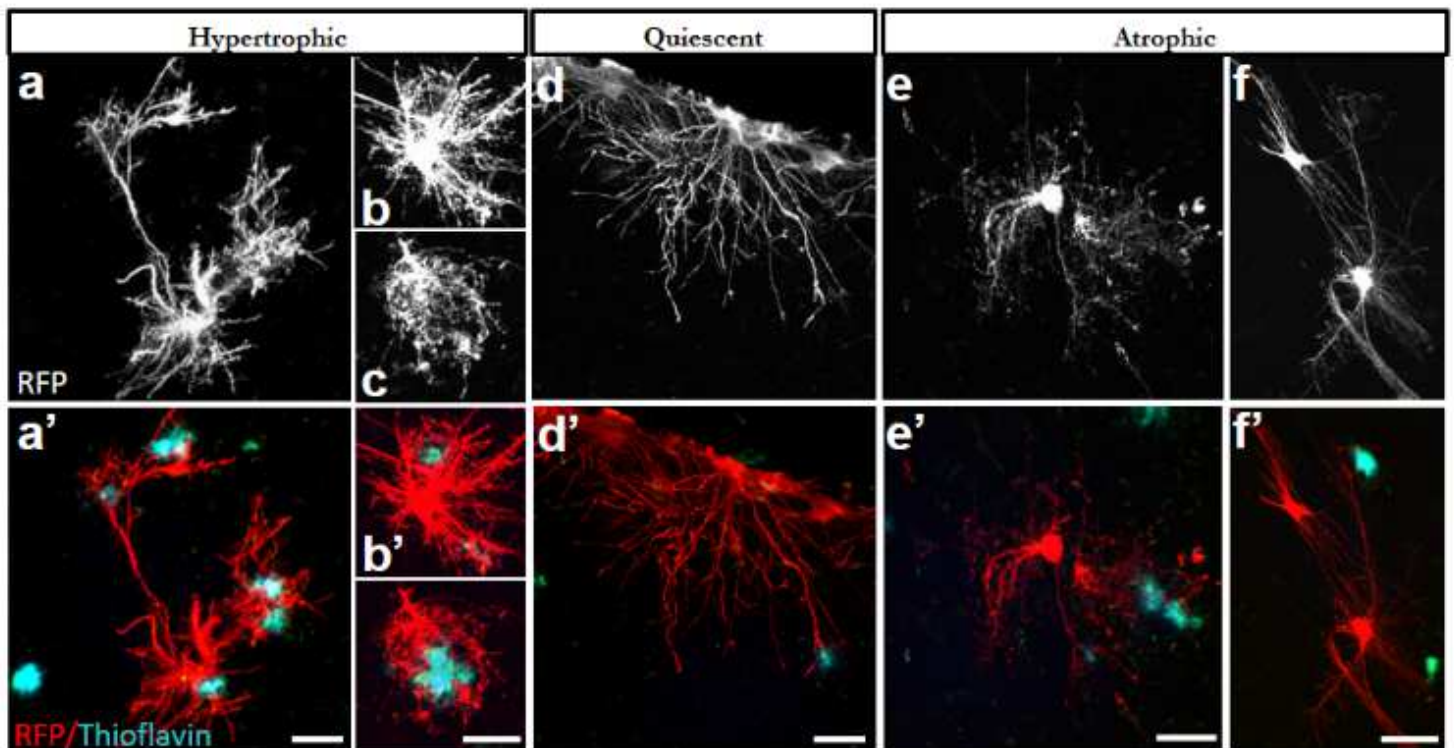
Figure 3

hiPSC-astrocytes recapitulate human morphological subtypes and retain human specific features within the mouse brain. (a-j) Representative images of RFP+ (white) interlaminar (a-c), varicose-projection (d-e), protoplasmic (f-g) and fibrous astrocytes (h-j) in the brain of wild-type mice five months after transplantation. Scale bars: 25 µm. (k) Histogram showing the percentage of RFP+ cells of each astroglial subtype on the mouse brain (n=9 mice). Data are represented as mean ± SEM. (l) Representative image showing mouse (green, arrows) and hiPSC-astrocytes (red) on a chimeric mouse brain five months after transplantation. Scale bar: 25 µm. (m) Histogram plotting the size of hiPSC-derived astrocytes vs mouse astrocytes on the host brain (n=12 mice). Data are represented as mean ± SEM, Student's t test: ****p<0.0001
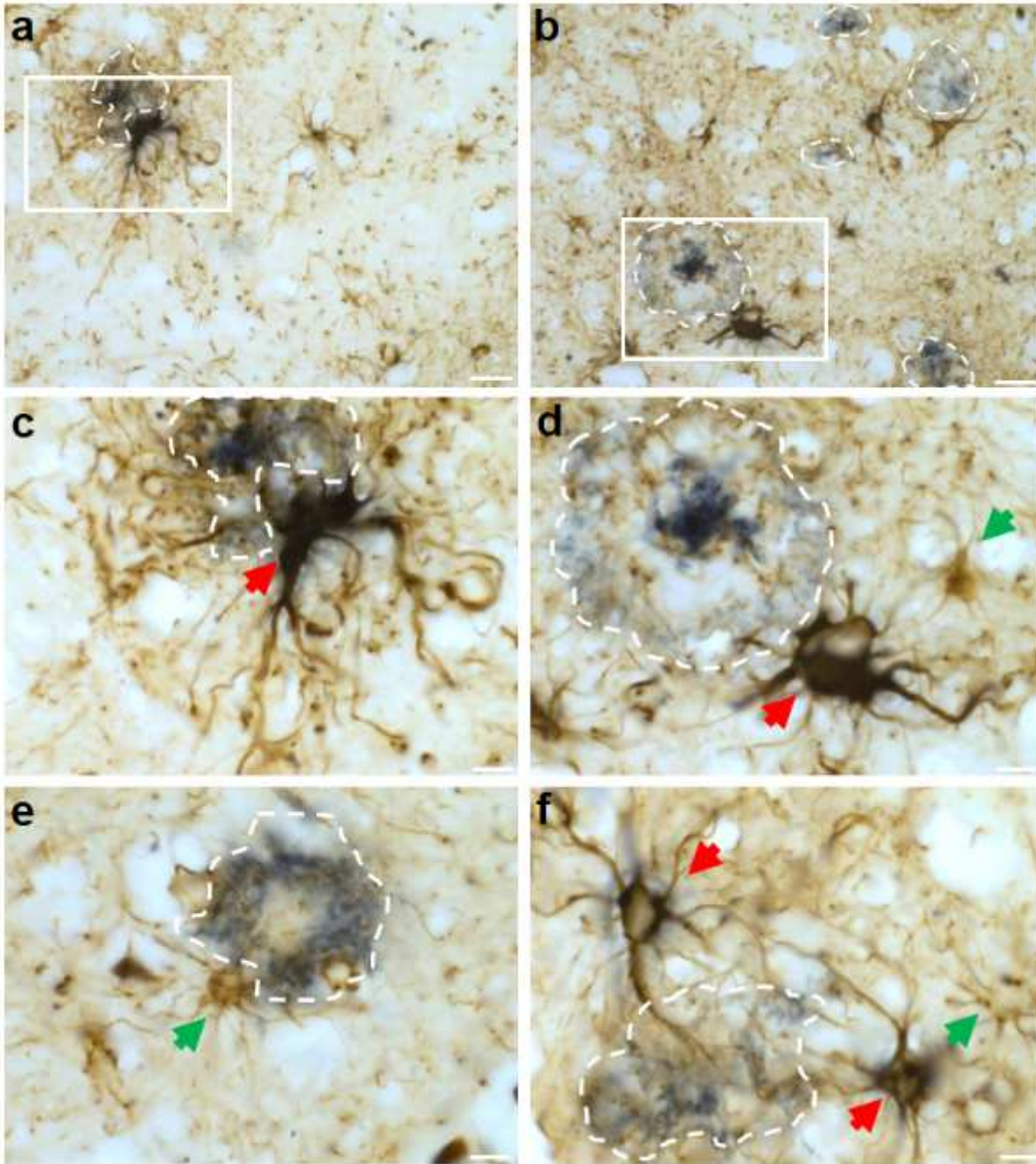
Figure 4

Four subtypes of morphologically defined GFAP+ astrocytes in the human entorhinal cortex and white matter. (a) Overview of human entorhinal cortex layers stained with GFAP (brown) to detect astrocytes. Layers molecular to lamina dissecans are mainly composed of subpial interlaminar astrocytes, while layers pri-α to pri-γ are rich in protoplasmic astrocytes (arrows). (b-f) Representative images of subpial interlaminar astrocytes (b) and their tortuous processes (c), protoplasmic astrocytes (d), varicose-projection astrocytes (e) and their beaded processes (f). (g-i) Overview of human white matter (g) and GFAP+ fibrous astrocytes (h-i). mol: molecular layer, diss: lamina dissecans. Scale bars: 50 μm in (a) and (g); 25 μm in (b) and (h); 10 μm in (c-f) and (i)

Figure 5

hiPSC-astrocytes show differential morphological responses to Aβ plaques within the chimeric mouse brain. (a-f, a'-f') hiPSC-astrocytes (RFP+, red) exposed to Aβ plaques (Thioflavin, green) show hypertrophic (a-c, a'-c'), quiescent (d, d') and atrophic (e-f, e'-f') morphologies in AD chimeric mice five months after transplantation. Scale bars: 25 μm. (g-h) Percentage of hiPSC-astrocytes showing differential morphologies as a group (g, n=7 mice) and per ApoE genotype (h, n=3 mice for APOE3/3; n=4 mice for APOE4/4) five months post- transplantation. Data are represented as mean ± SEM, Chi-square test: n.s., non-significant
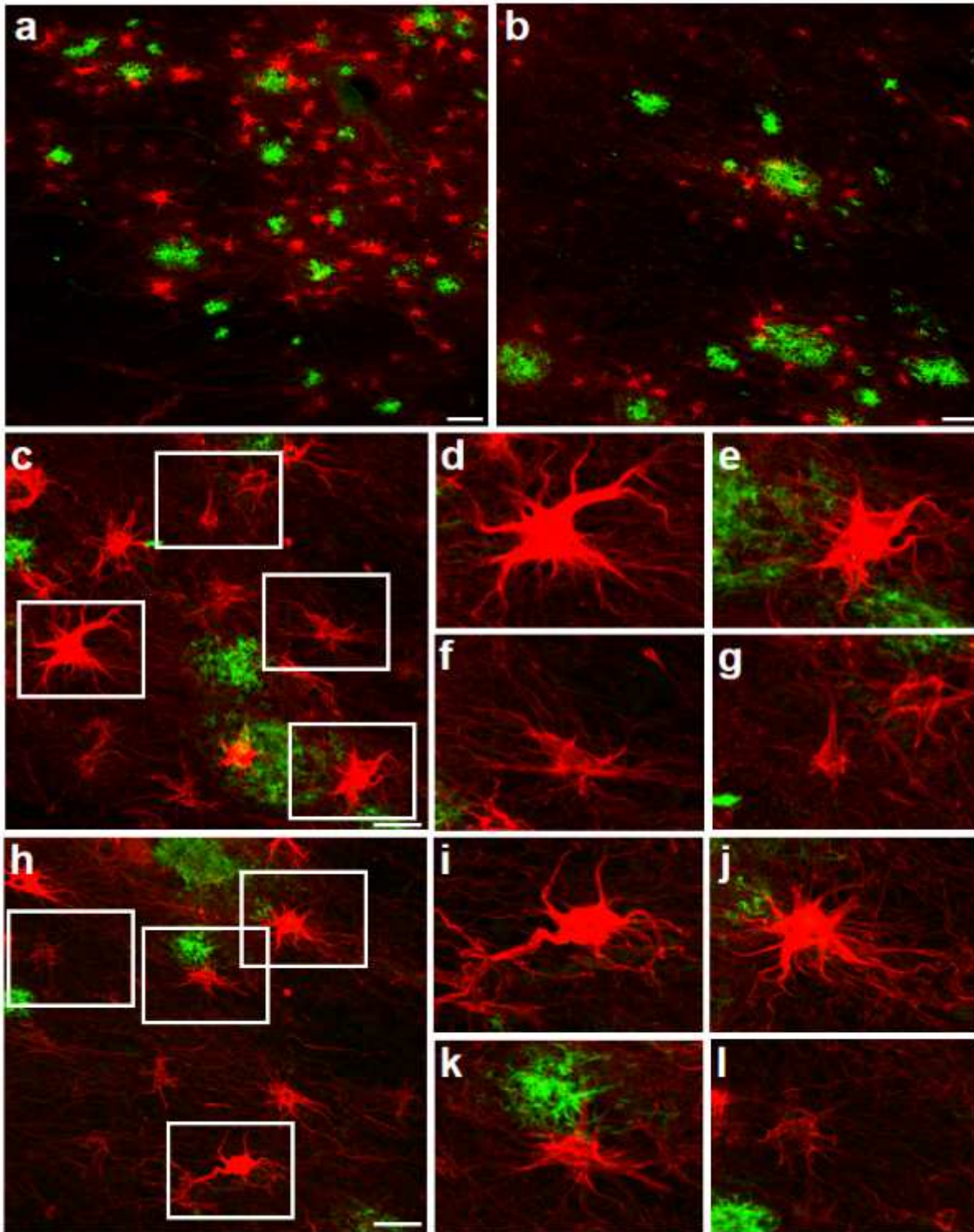

Figure 6

Astrocytes display differential responses to Aβ in the human AD-patient brain. (a- f) Representative immunohistochemistry images of GFAP+ astrocytes (brown) around amyloid-deposits (blue, dashed

lines) in the cortex and hippocampus of AD-patient brains. (a- d) Overviews (a, b) and enlarged views (c, d) of the insets in a, b respectively. (c-f) GFAP+ hypertrophic (red arrows) and quiescent or atrophic (green arrows) astrocytes around amyloid- deposits. Scale bars: 25 µm in (a, b); 10 µm in (c-f)

Figure 7

Hypertrophic, quiescent and atrophic astrocytes close to amyloid deposits in the human AD-patient brain. (a-l) Representative immunofluorescence images of GFAP+ astrocytes (red) around amyloid-deposits

(4G8, green) in the cortex and hippocampus of AD patient brains. (c-l) GFAP+ astrocytes (red) show hypertrophic (d-e, i-j), quiescent (f, k) and atrophic (g, l) morphologies close to amyloid deposits. (d-g, i-l) Enlarged views of the insets in c and h respectively. Scale bars: 50 µm in (a, b) and 25 µm in (c, h)

Supplementary Files

This is a list of supplementary files associated with this preprint. Click to download.

- Additionalfile1.TableS1.docx
- Additionalfile2.FigureS1.docx
- Additionalfile3.FigureS2.docx